

Article

Exploring the Spectral Line Broadening of the Bulk Motions in the High Mass Star Forming Region with Radiative Transfer Simulations

Shixian Mo ^{1,2}  and Keping Qiu ^{1,2,*} 

¹ School of Astronomy and Space Science, Nanjing University, 163 Xianlin Avenue, Nanjing 210023, China; mg20260009@smail.nju.edu.cn

² Key Laboratory of Modern Astronomy and Astrophysics, Nanjing University, Ministry of Education, Nanjing 210023, China

* Correspondence: kpqiu@nju.edu.cn

Abstract: The Davis–Chandrasekhar–Fermi (DCF) method is widely used to indirectly estimate the strength of magnetic fields in star-forming regions. However, recent developments in this method have primarily focused on improving the measurement of angular dispersion of the field, neglecting other physical quantities, especially turbulence velocity. Most DCF studies tend to overlook or fail to acknowledge the influence of bulk motions on the linewidth, and directly obtain the turbulence velocity based on the non-thermal linewidth. Therefore, to explore the contributions of bulk motions to the linewidth, we conducted radiative transfer simulations using a rotating and infalling envelope–disk model to a high-mass star formation region, IRAS18360-0537. The main conclusion from our work is that the bulk motions contribute significantly to the linewidth and cannot be fully eliminated by simply deducing velocity gradients. Hence, fully attributing the observed non-thermal velocity dispersion derived from fitting a spectral line profile to the turbulence can result in significantly overestimated magnetic field strength and may yield unscientific results of star-forming regions.

Keywords: radiative transfer simulation; bulk motion; turbulence velocity



Citation: Mo, S.; Qiu, K. Exploring the Spectral Line Broadening of the Bulk Motions in the High Mass Star Forming Region with Radiative Transfer Simulations. *Universe* **2023**, *9*, 415. <https://doi.org/10.3390/universe9090415>

Academic Editor: Jacco Th. van Loon

Received: 31 May 2023

Revised: 1 September 2023

Accepted: 7 September 2023

Published: 10 September 2023



Copyright: © 2023 by the authors. Licensee MDPI, Basel, Switzerland. This article is an open access article distributed under the terms and conditions of the Creative Commons Attribution (CC BY) license (<https://creativecommons.org/licenses/by/4.0/>).

1. Introduction

Interstellar turbulence is one of the significant factors that determine the density and velocity statistics of the interstellar medium. Consequently, it is widely considered to play a crucial role in the structure and evolution of galaxies, as well as in the process of star formation within molecular clouds [1–4]. The presence of super-Alfvénic turbulence is a key consideration in almost high-mass star-forming theories. Furthermore, several important physical quantities of star-forming regions are dependent on the turbulence velocity. For instance, the estimation of virial parameters is directly related to the turbulence velocity, and the star formation rate or the initial mass function model also depends on turbulence statistics. With the advancement of the interferometer telescope, magnetic fields are being increasingly detected in star-forming regions. The current high-mass star-forming theories suggest that turbulence and magnetic field are both important mechanisms to resist gravitational collapse in high-mass star formation, and which of them plays a more important role remains a hot topic of debate. Although there are more and more ways to detect high-resolution magnetic fields, such as the Zeeman effect [5,6], the Goldreich Kylafis (G-K) effect [7,8], and the Velocity Gradient Technique [9], these methods have more stringent applicable conditions. The dust grain polarized emission is still the main tracer of the magnetic field on molecular cloud, core, and envelope scales, where the polarization angles are perpendicular to the magnetic field orientations over large areas and a wide range of densities via the dust grains “radiative torque” (RAT) mechanism [10–12]. However, dust polarization can only reveal magnetic field morphologies and cannot tell us the

field strengths directly. Therefore, numerous methods have been developed for indirectly estimating the magnetic field strength from the field morphology, among which the Davis–Chandrasekhar–Fermi (DCF) method [13] and its derived methods are the most widely used ones despite long-standing theoretical concerns [14–16]. In the DCF method, the gas turbulence velocity is a necessary quantity to estimate the field strength, for the assumption that the turbulent energy and the energy of the turbulent component of the magnetic fields are in equal partitions. In other words, the observed distortion of the otherwise ordered field lines is caused by the turbulent motions. For a given turbulence velocity and gas density, the magnetic field strength can then be inferred with the following equation:

$$B_{pos} = f \sqrt{4\pi\rho} \frac{\sigma_v}{\delta\phi}, \quad (1)$$

where ρ is the gas density, σ_v is the turbulence velocity, and $\delta\phi$ represents the angular dispersion of magnetic field position angles. Ostriker et al. [17] suggested a factor of $f = 1/2$ to this estimation, considering the overlapping field in the line-of-sight direction based on superalfvenic MHD simulations to molecular clouds. Thereafter, subsequent studies of the modified DCF methods have been devoted to gaining a better angular dispersion measurement based on magnetic field morphologies. For example, Girart et al. [18] and Qiu et al. [19] fitted a set of parabolic field lines to remove the angular dispersion component caused by the highly regular “hourglass” shape field. For more complex magnetic field morphologies, the structure functions method and the angular dispersion function (ADF) method are applied to separate the large-scale and turbulent components of the fields [16,20–22]. Another approach to separating the turbulent field angular dispersion is to mimic the large-scale magnetic field by smoothing the field orientations within a chosen area. The spatial filtering technology [23] and unsharp masking technology [24] are two representative methods.

Researchers have consistently been engaged in discussions of angular dispersion measurements, although such intensive discussions introduce a relatively minor improvement in the accuracy of magnetic field strength estimation. Surprisingly, only a limited number of studies have concentrated on the measurement of turbulence velocity in molecular clouds. In the majority of studies employing the DCF method, turbulence velocities are typically determined by extracting the non-thermal gas velocity by fitting the linewidth of certain molecular spectral lines. It appears that there is a general lack of awareness or neglect regarding the influence of other factors on the spectral line width. For example, the non-thermal velocities can be susceptible to contamination from bulk motions, such as rotations, infalls, and outflows. Therefore, it is necessary to subtract the bulk motion components from the non-thermal velocity to accurately ascertain the turbulence velocity. A small fraction of the DCF studies have recognized this inaccuracy and, therefore, opted for an alternative approach, which involves deriving turbulence velocities from larger physical scale spectral line observations using empirical relationships [25–27]. The others qualitatively mention the broadening of the bulk motions. More meticulous works attempted to fit the velocity gradient caused by rotational and shearing motions in the first-moment map to separate bulk motions from turbulent motions quantitatively [28–30]. Nevertheless, this simple method lacks the capability to fully calculate the contribution of bulk motions along the line of sight. As a result, it may underestimate the influence of certain bulk motions, such as infalls. In summary, most DCF works do not recognize or adequately consider the impact of bulk motions in turbulence measurements. Such oversight might result in serious overestimation of turbulence velocities and magnetic field strengths, which might further cause the misjudgment of the relative significance of magnetic field, turbulence, and gravity, and then lead to unscientific results while determining properties of star-forming regions. Therefore, we further quantitatively investigate the component of bulk motions that contributed to the spectral linewidth with the radiative transfer simulations to a rotating and infalling envelope–disk model to compare the turbulence velocity calculated through current methods with the value incorporated in the model. This work

can also serve as a reminder to relevant researchers to exclude bulk motions in turbulence velocity measurement.

Our work is based on ALMA observation data of high-resolution CH₃OH(10_{2,9}-9_{3,9}) to the high-mass star-forming region IRAS 18360-0537. We find that considering only the bulk motions or turbulence is insufficient to explain the observed spectral lines. Therefore, the contributions of each in spectral lines are important and cannot be ignored. Section 2 describes the observations, the model, and the radiative transfer simulation setups. Sections 3 and 4 present the results of the simulation and discussions, respectively. We finally summarize our work in Section 5.

2. Observations and Model

The ALMA observations of the high-mass star-forming region IRAS18360-0537 (ID:2017.1.00793.S, PI: Zhang) were carried out in June 2018 using Band 6. In this work, we chose a baseband that covered the CH₃OH(10_{2,9}-9_{3,9}) transition at 233.89 GHz with a 0.17 km s⁻¹ velocity resolution. This line transition shows less morphological confusion and spectroscopic blending with other line emissions. The simultaneous 1.3 mm polarization observations of continuum emissions with a total bandwidth of 5.6 GHz are reported in subsequent research focusing on magnetic field analysis (in preparation). Table 1 lists the dates, number of antennas, calibrators, and on-source times of the observations. The typical flux uncertainty in ALMA observations was estimated to be ~10%. The calibrated UV data and images were processed using the Common Astronomy Software Applications (CASA [31], Version 5.4.0). The continuum image was constructed from line-free channels and the selected CH₃OH line also underwent baseline fitting. All images were synthesized using the ‘tclean’ task with a Briggs weighting parameter of 0.5. Additionally, primary beam correction was applied to each of the images. The continuum image has a synthesized beam size of 1.2'' × 1.3'' (P.A. = -56°) and a 1σ_{rms} noise level of 1.3 mJy beam⁻¹. The CH₃OH line cube has the synthesized beam of 1.16'' × 1.44'' (P.A. = -72°) and a noise level of 12 mJy beam⁻¹ in a 0.17 km s⁻¹ channel width. Figure 1 shows the velocity (first-moment map) and velocity dispersion (second-moment map) maps, where two identified condensations are asterisked.

Table 1. Observations parameters.

Date	Number of Antennas	On Source Time	Flux cal.	Phase cal.	Bandpass cal.
23 June 2018	47	6608	J1751 + 0939	J1851 + 0035	J1751 + 0939
23 June 2018	47	5569	J1751 + 0939	J1851 + 0035	J1751 + 0939
23 June 2018	47	6524	J1751 + 0939	J1851 + 0035	J1751 + 0939

We developed a molecular cloud model containing a protostar, an accretion disk, and a gas envelope with additional micro-turbulence and performed radiation transfer simulations to fit the observation data. The direct purpose of simulations was to investigate the contributions of bulk motions and turbulence to the spectral linewidth. It is important to note that our model may have been incomplete as we did not account for the potential influence of outflows and other forms of star-forming feedback. The outer boundary of the model was determined based on continuum observations, while the inner boundary was set at 50 AU to avoid zero points. The fundamental assumptions underlying this model were that energy and angular momentum are conserved during the infall process, and the self-gravity of the gas can be disregarded. As our primary focus was on the kinematic characteristics, the gas density distribution in this model was assumed to be spherically symmetric, with a simplified relationship of $\rho \propto r^{-1.5}$ for the envelope and $\rho \propto r^{-2.5}$ for the disk [32]. Additionally, the gas density remained continuous at the boundary between the disk and the envelope. The gas-to-dust mass ratio was taken to 100 and the scattering of dust was isotropic. We assumed the inner radius of the envelope was equal to the

radius of the centrifugal barrier, where the infall velocity diminishes to zero. The velocity components of the envelope can be expressed as follows:

$$v_{\psi,env} = v_0 \frac{r_0}{r}, \quad (2)$$

$$v_{r,env} = -\sqrt{\frac{2GM}{r} - v_{\psi,env}^2} = -v_0 \frac{\sqrt{r_0(r - r_0)}}{r}, \quad (3)$$

where $v_0 = \sqrt{2GM/r_0}$ is the rotation velocity at the inner envelope radius r_0 and M is the protostar mass. The rotation and infall velocity of the Keplerian disk are

$$v_{\psi,disk} = \sqrt{\frac{GM}{r}}, \quad (4)$$

$$v_{r,disk} = 0. \quad (5)$$

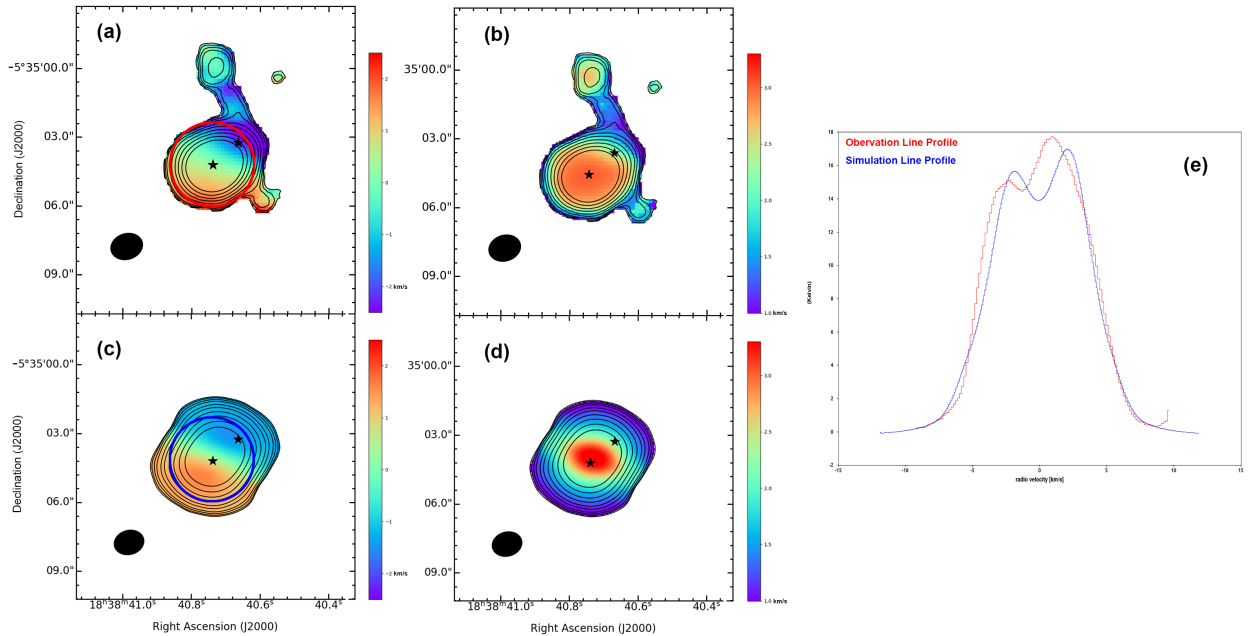


Figure 1. (a) Velocity field (color shades) of the $\text{CH}_3\text{OH}(10_{2,9}-9_{3,9})$ line emission with velocity-integrated emission (contours) starting from $0.23 \text{ Jy km s}^{-1}$ and increasing in steps of $0.20 \text{ Jy km s}^{-1}$. The asterisks mark the positions of the two condensations identified by dust emissions. A velocity gradient, with the redshifted emission in the southeast and blueshifted emission in the northwest, is seen across the envelope, as evidence of the rotation envelope. (b) Velocity dispersion maps (color shades) overlaid with velocity-integrated emission (contours). (c,d) Same as (a) and (b), but for the best fit of our model. The velocity dispersion map is unable to be perfectly fitted with our simple model and we alternatively match the average velocity dispersion. (e) The spectral line profile within the region of $2''$ radius (circled in the velocity field maps) for observations and our simulations.

We assumed that gas and dust were effectively coupled and had identical temperatures. The temperature profiles of the envelope and disk were derived from the ‘mcthem’ task, which is a Monte Carlo simulation code built in the package RADMC3D [33]. In the above temperature simulations, the two crucial free variables, namely the protostar radius and luminosity, were obtained from an inflated protostar model [34] with a given protostar mass. We took 400 logarithmic grids in a radius direction and 100×100 uniform grids in two different angular directions, resulting in a total of 4×10^6 grid points. We modeled the

spectral lines under the local thermodynamic equilibrium (LTE) assumption and assumed that the emissions were optically thin and the excitation conditions were universal across the region. The radiation transfer simulation was subsequently performed on the above model using version 2.0 of the RADMC3D code. The resulting output images and cubes were convolved with the ALMA instrumental response using version 5.4.0 of CASA. We produced an ALMA simulation observation using the CASA task ‘simobserve’ with the same observing conditions of the data. The obtained ALMA-simulation visibilities from the model images were further synthesized and primary-beam-corrected using task ‘tclean’ with the same weighting parameters of observations. The noise levels and beam sizes of the simulation and observed spectral line matched each other.

3. Results

To better compare the model spectra with those from the ALMA images, we set several parameters based on previous observations. The envelope outer radius and envelope mass are fixed to $r_{out}/d = 2''$ ($r_{out} \sim 12,600\text{AU}$ and $d \sim 6.3\text{ kpc}$) and $M = 80 M_{\odot}$ based on dust continuum images. We adopted the envelope’s half-cavity opening angle to be the same as that of the SiO and CO outflows of $\theta_h \sim 30^{\circ}$ [35]. To simplify our analysis, we assumed that the mass of the disk is one-third that of the protostar. As the gas density at the boundary remains consistent, the disk outer radius or envelope inner radius is determined by the protostar mass. The clear velocity gradient and the corresponding bipolar outflows indicate that the disk is approximately edge-on. Moreover, we carefully explored the simulation line profile under different inclination angles and found that the double-peak structure of spectral lines (see in Figure 1) exhibited more significant performance with large inclination angles. To enhance the reliability of the fitted protostar mass which is related to the double-peak line profile, we opted to fix the inclination angle at $i = 90^{\circ}$. Subsequently, we varied protostar mass ranging from $10 M_{\odot}$ to $80 M_{\odot}$ with an interval of $10 M_{\odot}$ and found the best-fit velocity map with the protostar mass of $60 M_{\odot}$, and the methanol abundance was fitted to match the flux of this transition with the observed data. The simulated gas temperature profile can be fitted with a two-stage power-law function, characterized by indices -1.0 and -0.4 , with a turning point at about 400 AU . As anticipated, the bulk motions make a substantial impact on the spectral linewidth and the line profile. This implies that there are significant challenges associated with attributing the spectral non-thermal linewidth solely to turbulence, as has been performed in most DCF research. However, we also noted that the linewidth cannot be solely attributed to the bulk motions, as relying solely on bulk motions is insufficient to restore the line profiles perfectly. Therefore, we also included turbulence velocity in the simulation. To obtain such a turbulence velocity component, we added gas micro-turbulence in the model to replace the macro cascade turbulence in the real molecular cloud. We emphasize that this approach is appropriate because our study does not aim to specifically investigate the influence of turbulence on linewidth at various scales. Rather, its objective is to analyze the contribution of turbulence to the broadening of the observed line at our specific observation scale. We explored the turbulence velocity v_{turb} across a range of $1.0\text{--}2.0\text{ km s}^{-1}$ with an interval of 0.1 km s^{-1} and determined the best-fit turbulence velocity of 1.4 km s^{-1} . Figure 1 shows the line profile and the moment maps of the best-fitting model and Table 2 presents the parameters for the disk and envelope models.

Table 2. Radiative transfer simulation parameters.

Model Parameters	Results
Protostar mass	60 M_{\odot}
Disk mass	20 M_{\odot}
Disk (centrifugal) radius	730 AU
Envelope mass ¹	80 M_{\odot}
Envelope radius ¹	12,600 AU
Envelope half cavity opening angle ²	30°
CH ₃ OH Abundance	6.0×10^{-7}
Turbulence velocity	1.4 km s ⁻¹

¹ From dust emission observations. ² Same as the outflow half-cavity opening angle.

4. Discussion

Some studies mention that the contributions of bulk motions to the linewidth can be reflected by the spectral velocity gradient. For example, Yue et al. [36] propose that the line dispersion can be decomposed into turbulence and bulk motion components such that $\sigma_v^2 = \sigma_{bm}^2 + \sigma_{turb}^2$. Based on this work, we can estimate the contribution of bulk motions with a more convenient calculation method,

$$\sigma_{bm}^2 = \sum_i^N (v_{bm} - \bar{v})^2 \frac{J_{bm}}{J}, \quad (6)$$

where $\bar{v} = \sum v_{bm}^2 J_{bm} / J$ is the mean velocity of the magnetic field detected region, J_{bm} refers to the spectral line integrated total intensity within a beam i and J is the sum of integrated intensities of the magnetic-field-detected region. We collected statistics on the velocity within the magnetic field detection region, resulting in the bulk motion velocity of 1.6 km s⁻¹. With the assumption that the bulk motion velocity has the same value in the line of sight, the turbulence velocity was calculated to be 2.2 km s⁻¹ after deducting the bulk motions, which is still 50% wider than the value in our simulations. Hence, a linear velocity gradient, commonly associated with rotation, cannot fully explain the underlying bulk motions. Other motions, particularly the infalling motion, may also significantly contribute to the observed linewidth. To further assess the importance of the infalling motion, we conducted a simulation using the same model but without the inclusion of infall motions. Figure 2 presents a comparison of the simulation results between the models with and without infall. While the disparity of the velocity maps between the two models is small, their spectral line profiles precisely exhibit substantial differences. Such differences can also be observed in their velocity dispersion maps. Through this straightforward simulation, we verified, as expected, that velocity gradients primarily reflect the rotational characteristics of the model while being unable to track the infall motions. Consequently, we proposed that in future research, the contribution of bulk motions to the observed linewidth cannot be eliminated by simply deducing velocity gradients.

Similarly, our model only incorporates an infalling and rotating envelope and a Keplerian disk, thereby excluding velocity broadening caused by outflows and other star-forming feedback. However, the molecules commonly employed to estimate turbulence velocity are generally less susceptible to such star-forming activities. As depicted in Figure 1, our simulations cannot perfectly fit the velocity dispersion map (second moment). This discrepancy may arise from the simplified density setting of our model as well as the omission of two detected dense condensations. Or rather, the simulated region does not manifest a perfect envelope–disk structure. Izquierdo [37] found that the inclination of the model also has a non-negligible impact on linewidth through the complex envelope and disk model simulations. We also simulated the case of smaller inclinations to the model and observed that a smaller inclination corresponded to a larger protostar mass. For instance, Figure 3 showcased a comparison of the simulation results between the best-fit model with the inclination angle of 90 and 70 degrees. It is evident that the double-peak

structure becomes less prominent at a smaller inclination as the minimum point moves up. Our simulation further demonstrates that to counterbalance this trend, a larger protostar mass is necessary. Based on this, we decided to fix the disk at an edge-on configuration to constrain the already large fitted protostar masses. Nonetheless, we successfully simulated the velocity map, the line profile, and the line width. We confirmed that the bulk motion broadening of spectral lines tracing high-density gas is significant and incomplete or failed removal of this component would significantly impact the accuracy of turbulence velocity detection. Therefore, it is crucial to carefully consider such an effect to avoid unscientific overestimation of the magnetic field strengths in the application of the DCF methods.

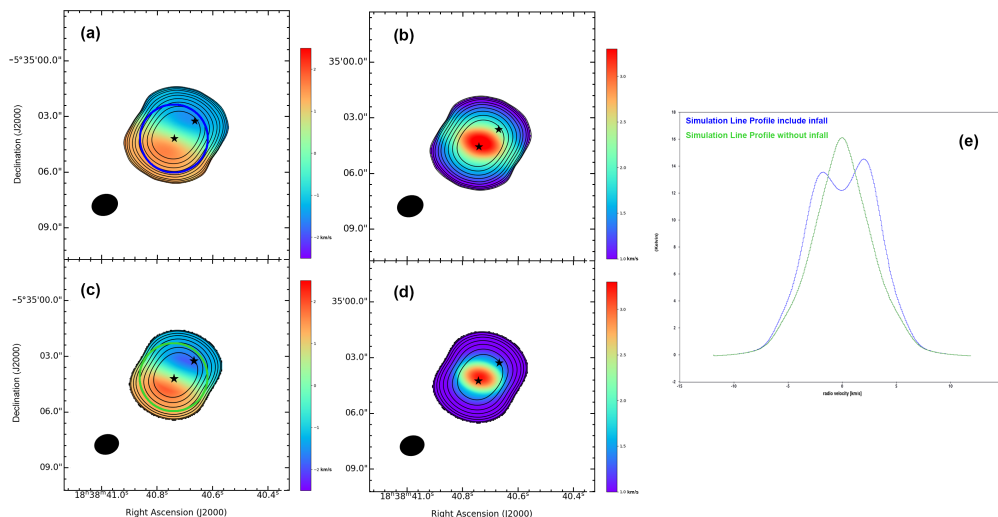


Figure 2. Same as Figure 1, but a comparison between the models with and without infalling motions. The velocity field between the two models is small. However, the model without infalling motions reveals smaller velocity dispersion and a significant difference in spectral line profile.

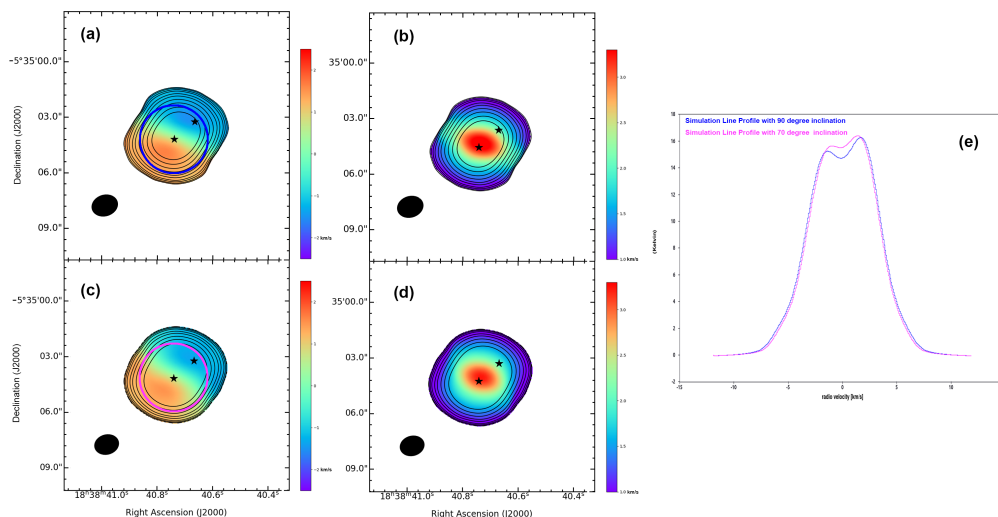


Figure 3. Same as Figure 1, but a comparison between the best-fit model with the inclination angle of 70 and 90 degrees. The double-peak structure becomes less prominent at a smaller inclination as the minimum point moves up.

5. Conclusions

We performed a radiative transfer simulation of the CH₃OH(10_{2,9}-9_{3,9}) spectral line with a model containing an infalling and rotating envelope, a Keplerian disk, and a high-mass protostar, and compared the simulation results to our ALMA observations. Our

simulation results show that the turbulence velocity is only about 1.4 km s^{-1} for an observed velocity dispersion of 2.7 km s^{-1} , and both motions and turbulence make significant contributions to the linewidth of spectral lines. Moreover, we concluded that line broadening caused by the infalling motions cannot be eliminated by simply subtracting the velocity gradient. Consequently, it is not feasible to derive the turbulence velocity simply by fitting an observed line profile, and effective methods must be employed to completely deduct the bulk motion velocities. Otherwise, severe overestimation of turbulence velocity occurs and renders the estimation of magnetic field intensity using the DCF method unreliable.

Author Contributions: Conceptualization, S.M. and K.Q.; software, S.M.; formal analysis, S.M.; data curation, S.M.; writing—original draft preparation, S.M.; writing—review and editing, S.M. and K.Q.; visualization, S.M.; supervision, K.Q. All authors have read and agreed to the published version of the manuscript.

Funding: S.M. and K.Q. are supported by National Key R&D Program of China No. 2022YFA1603100 and No. 2017YFA0402604, the National Natural Science Foundation of China (NSFC) grant U1731237, and the science research grant from the China Manned Space Project with No. CMS-CSST-2021-B06.

Data Availability Statement: The datasets generated during and/or analysed during the current study are available from the corresponding author on reasonable request.

Acknowledgments: We express our gratitude to the referees for their valuable and constructive comments, which have significantly enhanced the clarity of this paper.

Conflicts of Interest: The authors declare no conflict of interest.

References

1. Scalo, J.; Vázquez-Semadeni, E.; Chappell, D.; Passot, T. On the probability density function of galactic gas. I. Numerical simulations and the significance of the polytropic index. *Astrophys. J.* **1998**, *504*, 835. [[CrossRef](#)]
2. Mac Low, M.M.; Klessen, R.S. Control of star formation by supersonic turbulence. *Rev. Mod. Phys.* **2004**, *76*, 125. [[CrossRef](#)]
3. Elmegreen, B.G.; Scalo, J. Interstellar turbulence I: Observations and processes. *Annu. Rev. Astron. Astrophys.* **2004**, *42*, 211–273. [[CrossRef](#)]
4. McKee, C.F.; Ostriker, E.C. Theory of star formation. *Annu. Rev. Astron. Astrophys.* **2007**, *45*, 565–687. [[CrossRef](#)]
5. Crutcher, R.; Troland, T.; Goodman, A.; Heiles, C.; Kazes, I.; Myers, P. OH Zeeman observations of dark clouds. *Astrophys. J.* **1993**, *407*, 175. [[CrossRef](#)]
6. Crutcher, R.M.; Kemball, A.J. Review of zeeman effect observations of regions of star formation. *Front. Astron. Space Sci.* **2019**, *6*, 66. [[CrossRef](#)]
7. Goldreich, P.; Kylafis, N.D. On mapping the magnetic field direction in molecular clouds by polarization measurements. *Astrophys. J.* **1981**, *243*, L75–L78. [[CrossRef](#)]
8. Ching, T.C.; Lai, S.P.; Zhang, Q.; Yang, L.; Girart, J.M.; Rao, R. Helical magnetic fields in the NGC 1333 IRAS 4A protostellar outflows. *Astrophys. J.* **2016**, *819*, 159. [[CrossRef](#)]
9. González-Casanova, D.F.; Lazarian, A. Velocity gradients as a tracer for magnetic fields. *Astrophys. J.* **2017**, *835*, 41. [[CrossRef](#)]
10. Lazarian, A. Tracing magnetic fields with aligned grains. *J. Quant. Spectrosc. Radiat. Transf.* **2007**, *106*, 225–256. [[CrossRef](#)]
11. Hoang, T.; Lazarian, A. Grain alignment induced by radiative torques: Effects of internal relaxation of energy and complex radiation field. *Astrophys. J.* **2009**, *697*, 1316. [[CrossRef](#)]
12. Andersson, B.; Lazarian, A.; Vaillancourt, J.E. Interstellar dust grain alignment. *Annu. Rev. Astron. Astrophys.* **2015**, *53*, 501–539. [[CrossRef](#)]
13. Davis, L., Jr.; Greenstein, J.L. The polarization of starlight by aligned dust grains. *Astrophys. J.* **1951**, *114*, 206. [[CrossRef](#)]
14. Zweibel, E.G. Magnetic field-line tangling and polarization measurements in clumpy molecular gas. *Astrophys. J.* **1990**, *362*, 545–550. [[CrossRef](#)]
15. Myers, P.; Fuller, G.; Goodman, A.; Benson, P. Dense cores in dark clouds. VI-Shapes. *Astrophys. J.* **1991**, *376*, 561–572. [[CrossRef](#)]
16. Houde, M.; Vaillancourt, J.E.; Hildebrand, R.H.; Chitsazzadeh, S.; Kirby, L. Dispersion of Magnetic Fields in Molecular Clouds. II. *Astrophys. J.* **2009**, *706*, 1504. [[CrossRef](#)]
17. Ostriker, E.C.; Stone, J.M.; Gammie, C.F. Density, velocity, and magnetic field structure in turbulent molecular cloud models. *Astrophys. J.* **2001**, *546*, 980. [[CrossRef](#)]
18. Girart, J.M.; Rao, R.; Marrone, D.P. Magnetic fields in the formation of sun-like stars. *Science* **2006**, *313*, 812–814. [[CrossRef](#)]
19. Qiu, K.; Zhang, Q.; Menten, K.M.; Liu, H.B.; Tang, Y.W.; Girart, J.M. Submillimeter array observations of magnetic fields in g240.31+0.07: An hourglass in a massive cluster-forming core. *Astrophys. J. Lett.* **2014**, *794*, L18. [[CrossRef](#)]
20. Gonçalves, J.; Galli, D.; Girart, J.M. Modeling the magnetic field in the protostellar source NGC 1333 IRAS 4A. *Astron. Astrophys.* **2008**, *490*, L39–L42. [[CrossRef](#)]

21. Hildebrand, R.H.; Kirby, L.; Dotson, J.L.; Houde, M.; Vaillancourt, J.E. Dispersion of magnetic fields in molecular clouds. I. *Astrophys. J.* **2009**, *696*, 567. [[CrossRef](#)]
22. Houde, M.; Hull, C.L.; Plambeck, R.L.; Vaillancourt, J.E.; Hildebrand, R.H. Dispersion of magnetic fields in molecular clouds. IV. analysis of interferometry data. *Astrophys. J.* **2016**, *820*, 38. [[CrossRef](#)]
23. Pillai, T.; Kauffmann, J.; Tan, J.C.; Goldsmith, P.F.; Carey, S.J.; Menten, K.M. Magnetic fields in high-mass infrared dark clouds. *Astrophys. J.* **2015**, *799*, 74. [[CrossRef](#)]
24. Pattle, K.; Ward-Thompson, D.; Berry, D.; Hatchell, J.; Chen, H.R.; Pon, A.; Koch, P.M.; Kwon, W.; Kim, J.; Bastien, P.; et al. The JCMT BISTRO survey: The magnetic field strength in the orion a filament. *Astrophys. J.* **2017**, *846*, 122. [[CrossRef](#)]
25. Kandori, R.; Tomisaka, K.; Tamura, M.; Saito, M.; Kusakabe, N.; Nakajima, Y.; Kwon, J.; Nagayama, T.; Nagata, T.; Tatematsu, K. Distortion of Magnetic Fields in a Starless Core. IV. Magnetic Field Scaling on Density and Mass-to-flux Ratio Distribution in FeSt 1-457. *Astrophys. J.* **2018**, *865*, 121. [[CrossRef](#)]
26. Cortes, P.C.; Hull, C.L.; Girart, J.M.; Orquera-Rojas, C.; Sridharan, T.K.; Li, Z.Y.; Louvet, F.; Cortes, J.R.; Le Gouellec, V.J.; Crutcher, R.M.; et al. The seven most massive clumps in W43-Main as seen by ALMA: Dynamical equilibrium and Magnetic Fields. *Astrophys. J.* **2019**, *884*, 48. [[CrossRef](#)]
27. Arzoumanian, D.; Furuya, R.; Hasegawa, T.; Tahani, M.; Sadavoy, S.; Hull, C.; Johnstone, D.; Koch, P.; Inutsuka, S.I.; Doi, Y.; et al. Dust polarized emission observations of NGC 6334-BISTRO reveals the details of the complex but organized magnetic field structure of the high-mass star-forming hub-filament network. *Astron. Astrophys.* **2021**, *647*, A78. [[CrossRef](#)]
28. Myers, P. Dense cores in dark clouds. III-Subsonic turbulence. *Astrophys. J.* **1983**, *270*, 105–118. [[CrossRef](#)]
29. Federrath, C.; Rathborne, J.; Longmore, S.N.; Kruijssen, J.; Bally, J.; Contreras, Y.; Crocker, R.; Garay, G.; Jackson, J.; Testi, L.; et al. The link between turbulence, magnetic fields, filaments, and star formation in the central molecular zone cloud G0.253+0.016. *Astrophys. J.* **2016**, *832*, 143. [[CrossRef](#)]
30. Menon, S.H.; Federrath, C.; Klaassen, P.; Kuiper, R.; Reiter, M. On the compressive nature of turbulence driven by ionizing feedback in the pillars of the Carina Nebula. *Mon. Not. R. Astron. Soc.* **2021**, *500*, 1721–1740. [[CrossRef](#)]
31. McMullin, J.P.; Waters, B.; Schiebel, D.; Young, W.; Golap, K. CASA architecture and applications. In Proceedings of the Astronomical Data Analysis Software and Systems XVI, Tucson, TX, USA, 15–18 October 2006; ASP Conference Series 376; Shaw, R.A., Hill, F., Bell, D. J., Eds.; ASP: San Francisco, CA, USA, 2007; p. 127.
32. Zhang, Y.; Tan, J.C.; Sakai, N.; Tanaka, K.E.; De Buizer, J.M.; Liu, M.; Beltrán, M.T.; Kratter, K.; Mardones, D.; Garay, G. An Ordered Envelope–Disk Transition in the Massive Protostellar Source G339. 88-1.26. *Astrophys. J.* **2019**, *873*, 73. [[CrossRef](#)]
33. Dullemond, C.; Juhasz, A.; Pohl, A.; Sereshti, F.; Shetty, R.; Peters, T.; Commercon, B.; Flock, M. RADMC-3D: A Multi-Purpose Radiative Transfer Tool. *Astrophys. Source Code Libr.* **2012**, ascl:1202.015. Available online: <https://ui.adsabs.harvard.edu/abs/2012ascl.soft02015D/abstract> (accessed on 30 May 2023).
34. Hosokawa, T.; Yorke, H.W.; Omukai, K. Evolution of massive protostars via disk accretion. *Astrophys. J.* **2010**, *721*, 478. [[CrossRef](#)]
35. Qiu, K.; Zhang, Q.; Beuther, H.; Fallscheer, C. Forming an O Star via Disk Accretion? *Astrophys. J.* **2012**, *756*, 170. [[CrossRef](#)]
36. Yue, N.N.; Li, D.; Zhang, Q.Z.; Zhu, L.; Henshaw, J.; Mardones, D.; Ren, Z.Y. Resolution-dependent subsonic non-thermal line dispersion revealed by ALMA. *Res. Astron. Astrophys.* **2021**, *21*, 024. [[CrossRef](#)]
37. Izquierdo, A.F.; Galván-Madrid, R.; Maud, L.T.; Hoare, M.G.; Johnston, K.G.; Keto, E.R.; Zhang, Q.; de Wit, W.J. Radiative transfer modelling of W33A MM1: 3D structure and dynamics of a complex massive star-forming region. *Mon. Not. R. Astron. Soc.* **2018**, *478*, 2505–2525. [[CrossRef](#)]

Disclaimer/Publisher’s Note: The statements, opinions and data contained in all publications are solely those of the individual author(s) and contributor(s) and not of MDPI and/or the editor(s). MDPI and/or the editor(s) disclaim responsibility for any injury to people or property resulting from any ideas, methods, instructions or products referred to in the content.